

# Numerical aspects of Casimir energy computation in acoustic scattering

Timo Betcke<sup>a</sup>, Alexander Strohmaier<sup>b</sup>, Xiaoshu Sun<sup>a,\*</sup>

<sup>a</sup>*Department of Mathematics, University College London, London, WC1E 6BT, UK*

<sup>b</sup>*School of Mathematics, University of Leeds, Leeds, LS2 9JT, UK*

---

## Abstract

Computing the Casimir energy is a classical problem of quantum electrodynamics going back to the 1940s. In the early two thousands a significant breakthrough was achieved by representing the Casimir energy as the computation of the integral of the log determinant of certain boundary integral operators in the complex plane. Recently, this log determinant formula was investigated in the context of the Krein spectral shift function, which suggests a potential alternative computational approach based on the numerical evaluation of scattering matrices. In this paper, we will give an overview of these computational techniques of computing the Casimir energy in three dimensional acoustic scattering. Afterwards, we will discuss the spectral properties of the block matrices inside the formula of the Casimir energy, which are constructed by the integral operators and investigate how to use these properties to speed up Casimir computations for large-scale practical problems.

*Keywords:* Krein spectral shift function, Casimir energy, Krylov subspace, inverse-free generalized eigenvalue problem, Bempp

---

## 1. Introduction

Since late 1940s, the advanced understanding of vacuum sector of quantum electrodynamics has been developed and one of the most seminal predictions is the vacuum effects (quantum fluctuations of the electromagnetic field) can induce attractive forces between two uncharged, perfectly conducting, parallel plates. This phenomenon is called *Casimir effect*, which is firstly proposed by H.B.G. Casimir in 1940s [1]. To obtain the formula of the Casimir energy, he considered the space between these two plates as a type of electromagnetic cavity, solved the classical Maxwell equations with certain boundary condition for all the valid excitations of the electromagnetic field in this cavity and obtained countably infinite electromagnetic mode frequencies  $\{\omega_n(a)\}$ , where  $a$  is the surface-surface distance. Accordingly, the electromagnetic zero-point energy of the  $n$ th cavity mode is  $\frac{\hbar\omega_n(a)}{2}$  and by summing up all the contributions from the modes, he finally get the expression of the *Casimir energy*:

$$\mathcal{E}(a) = \frac{1}{2} \sum_n \hbar\omega_n(a),$$

which is divergent. However, Casimir derived a finite result for the derivative of this infinite energy fluctuations, which is the *Casimir force per unit area*:

$$F(a) = -\frac{1}{A} \frac{\partial \mathcal{E}}{\partial a} = -\frac{\hbar c \pi^2}{240 a^4},$$

where  $A$  is the cross-sectional area of the boundary plates.

In 1960s, Lifshitz generalized this theory to the case of dielectric media [2], which means the boundary surfaces are not perfect conductors but the real-world materials such us the solid consisting of the atomic

---

\*Corresponding author

URL: [t.betcke@ucl.ac.uk](mailto:t.betcke@ucl.ac.uk) (Timo Betcke), [a.strohmaier@leeds.ac.uk](mailto:a.strohmaier@leeds.ac.uk) (Alexander Strohmaier), [xiaoshu.sun.18@ucl.ac.uk](mailto:xiaoshu.sun.18@ucl.ac.uk) (Xiaoshu Sun)

constituents. He proposed that any microscopic volume  $\Delta V$  of the plates contains a collection of atomic-scale electric dipoles without uniform orientation due to the absence of the external forcing field. Once in a while, the quantum and thermal fluctuations may make the dipoles align spontaneously, resulting in a net electric dipole moment. It is like van der Waals interaction between the atoms and this dipole moment induces a net dipole field. Meanwhile, the dipoles in the opposite plate feel this field across the gap and align as well. Now, there are two net electric dipole moments which make two plates attract with each other. Lifshitz emphasized the influence from the materials more than the fluctuations in the empty space between the plates and this interpretation provides little advantage on the computation of the Casimir energy since it is unknown on how to compute each contribution from the volume  $\Delta V$ .

Afterwards, there is a decades absence of experimental input on the Casimir effect and finally in 1996, the precise measurements of the Casimir force between the extended bodies have been done by S.K. Lamoreaux [3]. From 2000 to 2008, the Casimir force has been measured in various experimental configurations, such as cylinder-cylinder [4], plate-plate [5], sphere-plate [6] and sphere-comb [7]. The rapid growth in experimental investigation is followed by the theoretical development. From 2007 to 2008, the asymptotic series of the Casimir energy have been explicitly computed by T. Emig's team in both scalar [8] and vector [9] cases. In 2009, Johnson's team put forward a method of computing the Casimir interactions between arbitrary three-dimensional objects with arbitrary material properties [10], in which the Casimir energy between the perfectly conducting compact objects can be described as:

$$\mathcal{E} = -\frac{\hbar c}{2\pi} \int_0^\infty dk \log \frac{\mathcal{Z}(k)}{\mathcal{Z}_\infty(k)},$$

where

$$\mathcal{Z}(k) = \int \mathcal{D}\mathbf{J}(\mathbf{x}) e^{\frac{1}{2} \int \int d\mathbf{x} d\mathbf{y} \mathbf{J}(\mathbf{x}) \cdot \mathbf{G}_k(\mathbf{x}, \mathbf{y}) \cdot \mathbf{J}(\mathbf{y})} \quad (1)$$

is a functional integration extending over all possible surface current distributions  $\mathbf{J}(\mathbf{x})$  on the objects and  $\mathcal{Z}_\infty(k)$  is  $\mathcal{Z}(k)$  computed with all the objects removed to infinite separation. Moreover, in (1),

$$\mathbf{G}_k(\mathbf{x}, \mathbf{y}) = \left[ 1 + \frac{1}{k^2} \nabla_{\mathbf{x}} \otimes \nabla_{\mathbf{y}} \right] \frac{e^{ik|\mathbf{x}-\mathbf{y}|}}{4\pi|\mathbf{x}-\mathbf{y}|}$$

is the dyadic/tensor Green's function and  $k$  is the wavenumber. Johnson proposed that one could formally apply contour integral arguments to obtain the integral along the imaginary axis on which the integrand is nicely behaved (non-oscillatory and exponentially decaying). In this case, the Casimir energy formula is rewritten as

$$\mathcal{E} = -\frac{\hbar c}{2\pi} \int_0^\infty dk \log \frac{\mathcal{Z}(ik)}{\mathcal{Z}_\infty(ik)}, \quad (2)$$

where

$$\mathcal{Z}(ik) = \int \mathcal{D}\mathbf{J}(\mathbf{x}) e^{\frac{1}{2} \int \int d\mathbf{x} d\mathbf{y} \mathbf{J}(\mathbf{x}) \cdot \mathbf{G}_{ik}(\mathbf{x}, \mathbf{y}) \cdot \mathbf{J}(\mathbf{y})} \quad (3)$$

and

$$\mathbf{G}_{ik}(\mathbf{x}, \mathbf{y}) = \left[ 1 - \frac{1}{k^2} \nabla_{\mathbf{x}} \otimes \nabla_{\mathbf{y}} \right] \frac{e^{-k|\mathbf{x}-\mathbf{y}|}}{4\pi|\mathbf{x}-\mathbf{y}|}.$$

This  $\mathbf{G}_{ik}$  is called the Wick-rotated dyadic/tensor Green's function. One can notice that this Green's function is strongly singular due to the second order form  $(\nabla_{\mathbf{x}} \otimes \nabla_{\mathbf{y}})$ .

However, a more rigorous mathematical derivation was recently provided by Hanisch, Strohmaier and Waters [11] who have shown that the natural and well-defined object is the integral along the imaginary axis. They

also provided a mathematical framework to connect the integral to families of trace formulas and the Casimir energy is one of the examples. To be specific, by assuming that the objects  $\Omega$  is assembled from individual objects  $\Omega_j$ , for  $j = 1, \dots, N$  and  $\partial\Omega_j$  are the  $N$  connected components of the boundary  $\partial\Omega$ . Then, several self-adjoint operators on  $L^2(\mathbb{R}^d)$  can be defined for constructing the *Birman-Krein formula* later:

- The operator  $\Delta$  is the Laplace operator with Dirichlet boundary conditions on  $\partial\Omega$ .
- For  $j = 1, \dots, N$ , the operator  $\Delta_j$  is the Laplace operator with Dirichlet boundary conditions on  $\partial\Omega_j$ .
- The operator  $\Delta_0$  is the ‘free’ Laplace operator on  $\mathbb{R}^d$  with domain  $H^2(\mathbb{R}^d)$ .

Now, the Birman-Krein formula can be written as

$$\text{Tr} \left( f(\Delta^{\frac{1}{2}}) - f(\Delta_0^{\frac{1}{2}}) - \left( \sum_{j=1}^N [f(\Delta_j^{\frac{1}{2}}) - f(\Delta_0^{\frac{1}{2}})] \right) \right) = \int_0^\infty f'(k)\xi(k)dk, \quad (4)$$

where

$$\xi(k) = \frac{1}{2\pi i} \log \left( \frac{\det(S(k))}{\det(S_{1,k}) \cdots \det(S_{N,k})} \right)$$

is called the *Krein spectral shift function* (KSSF). Here,  $S_{j,k}$  are the scattering matrices of  $\Delta_j$  associated to the objects  $\Omega_j$ .

According to [11], by setting  $f(x) = x$ , (4) becomes

$$\text{Tr} \left( \Delta^{\frac{1}{2}} + (N-1)\Delta_0^{\frac{1}{2}} - \sum_{j=1}^N \Delta_j^{\frac{1}{2}} \right) = \int_0^\infty \xi(k)dk \quad (5)$$

and the value of the integral in (5) is the Casimir energy. However, this integral is not Lebesgue integrable and therefore cannot be used to compute the energy. To solve this problem, the authors derivate a relation between the KSSF and the integral operators and finally make the Casimir energy numerically computable via the integral operator method.

In this paper, we are going to introduce the numerical framework of computing the Casimir energy based on the evaluation of the log determinant of the integral operators in the acoustic case <sup>1</sup> in Section 2 and discuss the spectral properties of the block matrices constructed from the integral operators in Section 3. Afterwards, with these properties, two efficient methods for computing the integrand of the Casimir energy will be illustrated in Section 4 which makes us compute the large-scale problem efficiently. In Section 5, several examples on computing the Casimir energy between the compact objects will be shown and we will also compare our results with others computed in other methods. Note that all the tests and examples in this paper were computed with version 3.3.4 of the BEM++ library [12]. Finally, Section 6 will conclude our paper and discuss the future plan as well.

## 2. Numerical methods for computing the Casimir energy in acoustic scattering

In this section, we are going to investigate the numerical methods on computing the Casimir energy. We would like to use the following notations for the domains of the boundary integral operators in both scalar and vector case. Assume  $\Omega^- \in \mathbb{R}^d$ , for  $d \geq 2$  is the interior bounded Lebesgue-measurable domain that the scatterer occupies with Lipschitz-continuous boundary  $\Gamma$  and  $\Gamma := \partial\Omega$  has a finite number of smooth faces that meet

---

<sup>1</sup>The mathematical theories and numerical experiments in the Maxwell case have been done as well and they will be reported in another paper.

at non-degenerate edges and corners. In addition, the exterior domain is denoted as  $\Omega^+ = \mathbb{R}^d \setminus \overline{\Omega^-}$ .  $\mathbf{n}$  is the exterior unit normal to the surface  $\Gamma$  pointing outwards from  $\Omega^-$  and  $\mathbf{n}_x$  is normal to  $\Gamma$  at the point  $x \in \Gamma$ .

In the scalar case, the Casimir energy can be expressed in terms of the single-layer boundary operator and we will start from defining the function space on which the boundary operators are well-defined and Dirichlet trace operator, then give the definition of the single-layer boundary operator. Afterwards, the relation between the Krein spectral shift function with this operator will be introduced and finally, the numerical framework for computing the Casimir energy in the scalar case via the Galerkin discretization of the single-layer boundary operator.

### 2.1. Scalar function space and trace operator

For the bounded interior domain  $\Omega^\pm$  or the unbounded exterior domain  $\Omega^+$ , the space of the square integrable functions is

$$L^2(\Omega^\pm) := \left\{ f : \Omega^\pm \rightarrow \mathbb{C}, f \text{ is Lebesgue measurable and } \int_{\Omega^\pm} |f|^2 < \infty \right\}$$

and the Sobolev space  $H^s(\Omega^\pm)$  is defined as

$$H^s(\Omega^\pm) := \left\{ f \in L^2(\Omega^\pm), \forall \alpha \text{ s.t. } |\alpha| \leq s, D^\alpha f \in L^2(\Omega^\pm) \right\},$$

where  $\alpha = (\alpha_1, \alpha_2, \dots, \alpha_d)$  is a multi-index and  $|\alpha| = \alpha_1 + \alpha_2 + \dots + \alpha_d$ , and the derivative is defined in the weak sense.

To construct the single-layer boundary operator, we also need the Dirichlet trace operator  $\gamma_D^\pm : H^1(\Omega^\pm) \rightarrow H^{\frac{1}{2}}(\Gamma)$ : for sufficiently smooth function  $p$ ,

$$\gamma_D^\pm p(\mathbf{x}) := \lim_{\Omega^\pm \ni \mathbf{x}' \rightarrow \mathbf{x} \in \Gamma} p(\mathbf{x}'),$$

where the subscripts  $-$  and  $+$  denote the interior and exterior traces, respectively.

### 2.2. Single-layer boundary integral operator

Typically, the *single-layer potential operator*  $\mathcal{V}_k : H^{-\frac{1}{2}}(\Gamma) \rightarrow H^1(\Omega^\pm)$  can be represented as

$$(\mathcal{V}_k \mu)(\mathbf{x}) := \int_\Gamma g_k(\mathbf{x}, \mathbf{y}) \psi(\mathbf{y}) dS_y, \quad \text{for } \mu \in H^{-\frac{1}{2}}(\Gamma) \text{ and } \mathbf{x} \in \Omega^\pm \setminus \Gamma,$$

where  $g_k(\mathbf{x}, \mathbf{y})$  is the fundamental solution of the Helmholtz operator and especially,

$$g_k(\mathbf{x}, \mathbf{y}) = \begin{cases} \frac{i}{4} H_0^{(1)}(k|\mathbf{x} - \mathbf{y}|), & \text{for } d = 2 \\ \frac{e^{ik|\mathbf{x} - \mathbf{y}|}}{4\pi|\mathbf{x} - \mathbf{y}|}, & \text{for } d = 3, \end{cases}$$

where  $H_0^{(1)}$  is a Hankel function of the first kind.

Now we can derive the *single-layer boundary operator*  $V_k : H^{-\frac{1}{2}}(\Gamma) \rightarrow H^{\frac{1}{2}}(\Gamma)$  from this potential operator:

$$(V_k \mu)(\mathbf{x}) := \{\gamma_D \mathcal{V}_k \mu\}_\Gamma(\mathbf{x}).$$

Combining with the jump condition

$$[\gamma_D]_\Gamma \mathcal{V}_k = \gamma_D^+ \mathcal{V}_k - \gamma_D^- \mathcal{V}_k = 0,$$

we can derive that

$$\gamma_D^+ \mathcal{V}_k = \gamma_D^- \mathcal{V}_k = V_k,$$

for the exterior and interior traces and the single-layer boundary operator writes

$$(V_k \mu)(\mathbf{x}) := \int_\Gamma g_k(\mathbf{x}, \mathbf{y}) \psi(\mathbf{y}) dS_y, \quad \text{for } \mu \in H^{-\frac{1}{2}}(\Gamma) \text{ and } \mathbf{x} \in \Gamma.$$

### 2.3. Relation between the Krein spectral shift function and the single-layer boundary operator

By [11], the Krein spectral shift function is defined as

$$\xi(k) = \frac{1}{2\pi i} \log \left( \frac{\det(S(k))}{\det(S_{1,k}) \cdots \det(S_{N,k})} \right),$$

where  $S_{i,n}$  is the scattering matrix associated with the  $n$ th scatterer. These scattering matrices can be constructed  $S_{i,n} = I + T_{i,n}$ , where  $I$  is the identity matrix and  $T_{i,n}$  is the  $T$ -matrix and the method of computing the  $T$ -matrix is fully discussed in [13] and [14].

The following theorem links the single-layer boundary operator with the Krein spectral shift function which inspires us to computing the Casimir energy via the scattering matrix or integral operator.

**Theorem 1.** [11] Consider  $\Omega$  as a domain assembling from individual objects  $\Omega_i$ . Let  $V_k$  be the single-layer boundary operator defined on the boundary  $\partial\Omega = \bigcup_{i=1}^N \partial\Omega_i$ , and  $\tilde{V}_k$  is the “diagonal part” of  $V_k$  by restricting the integral kernel to the subset  $\bigcup_{i=1}^N \partial\Omega_i \times \partial\Omega_i \subset \partial\Omega \times \partial\Omega$  then the operator  $V_k \tilde{V}_k^{-1}$  is trace-class and

$$\Xi(k) = \log \det(V_k \tilde{V}_k^{-1}).$$

Then for  $k > 0$ , we have

$$-\frac{1}{\pi} \operatorname{Im} \Xi(k) = \frac{i}{2\pi} (\Xi(k) - \Xi(-k)) = \xi(k)$$

and by choosing  $f(x) = x$  in (4), this gives the formula

$$\operatorname{Tr} \left( \Delta^{\frac{1}{2}} + (N-1)\Delta_0^{\frac{1}{2}} - \sum_{i=1}^N \Delta_j^{\frac{1}{2}} \right) = \int_0^\infty \xi(k) dk = -\frac{1}{\pi} \int_0^\infty \Xi(ik) dk. \quad (6)$$

The equation (6) is used to compute the Casimir energy between the objects and the formula is written as

$$\mathcal{E} = \frac{\hbar c}{2} \int_0^\infty \xi(k) dk = -\frac{\hbar c}{2\pi} \int_0^\infty \Xi(ik) dk \quad (7)$$

**Remark 1.** Note that the integral  $\frac{\hbar c}{2} \int_0^\infty \xi(k) dk$  in (7) is not Lebesgue convergence but might be Riemann integrable. Therefore, one should compute Casimir energy via the integral operator method but not the scattering matrix method.

### 2.4. Galerkin discretization and boundary element spaces

In order to compute the integral (7), we need to compute the log determinant of the operators  $V_k \tilde{V}_k^{-1}$ . In our numerical framework, we would like to use the Galerkin discretization to express the operators in matrix form and in this part, the explicit form of the element inside the matrix will be given and the Corresponding basis functions will be introduced as well.

Recall the domain of the single-layer boundary operator is  $H^{-\frac{1}{2}}(\Gamma)$ . To discretize this Sobolev space, we would like to introduce the triangulation  $\mathcal{T}_h$  of the boundary surface  $\Gamma$  with triangular surface elements  $\tau_l$  and associated nodes  $\mathbf{x}_i$  s.t.  $\overline{\mathcal{T}_h} = \bigcup_l \overline{\tau_l}$ , where  $h$  is the mesh size and define the space of the continuous piecewise linear functions

$$P_h^1(\Gamma) = \{v_h \in C^0(\Gamma) : v_h|_{\tau_l} \in \mathbb{P}_1(\tau_l), \text{ for } \tau_l \in \mathcal{T}_h\},$$

where  $\mathbb{P}_1(\tau_l)$  denotes the space of polynomials of order less than or equal to 1 on  $\tau_l$  and typically, we use the following  $P_h^1(\Gamma)$  space to discretize  $H^{-\frac{1}{2}}(\Gamma)$ :

$$P_h^1(\Gamma) := \operatorname{span}\{\phi_j\} \subset H^{-\frac{1}{2}}(\Gamma)$$

with

$$\phi_j(\mathbf{x}_i) = \begin{cases} 1, & i = j, \\ 0, & i \neq j. \end{cases}$$

Having defined the basis function  $P_h^1(\Gamma)$ , we can represent each element inside the Galerkin discretization form. Assume there are  $N$  objects, then the matrix of the operator  $V_k$  is an  $N$  by  $N$  block matrix, written as

$$V_k = V(k) = \begin{bmatrix} V_{11}(k) & V_{12}(k) & \cdots & V_{1N}(k) \\ V_{21}(k) & V_{22}(k) & \cdots & V_{2N}(k) \\ \vdots & \vdots & \ddots & \vdots \\ V_{N1}(k) & V_{N2}(k) & \cdots & V_{NN}(k) \end{bmatrix}$$

and the matrix  $\tilde{V}_k$  is the diagonal part of  $V_k$ :

$$\tilde{V}_k = \tilde{V}(k) = \begin{bmatrix} V_{11}(k) & 0 & \cdots & 0 \\ 0 & V_{22}(k) & \cdots & 0 \\ \vdots & \vdots & \ddots & \vdots \\ 0 & 0 & \cdots & V_{NN}(k) \end{bmatrix}.$$

Therefore, the element in the  $m$ th row and  $n$ th column of the block matrix  $V_{ij}(k)$  is

$$V_{ij}^{(m,n)}(k) = \langle V_{ij}(k)\phi_m^{(i)}, \phi_n^{(j)} \rangle = \int_{\Gamma} \overline{\phi_n^{(j)}(\mathbf{x})} \int_{\Gamma} g_k(\mathbf{x}, \mathbf{y}) \phi_m^{(i)}(\mathbf{y}) dS_{\mathbf{y}} dS_{\mathbf{x}}, \quad (8)$$

where  $\boldsymbol{\phi}^{(i)} = [\phi_1^{(i)} \quad \phi_2^{(i)} \quad \dots \quad \phi_N^{(i)}]$  is the set of basis functions defined on the  $i$ th object and

$$\langle f, g \rangle = \int_{\Gamma} \overline{f(\mathbf{x})} g(\mathbf{x}) dS_x$$

denotes the standard  $L^2(\Gamma)$  inner product.

By (8), the explicit form of each element in matrix  $V$  and  $\tilde{V}_k$  is known, therefore, the value of  $\Xi(ik) = \log \det(V_{ik}\tilde{V}_{ik}^{-1})$  can be evaluated by computing  $\log \frac{\det V_{ik}}{\det \tilde{V}_{ik}}$  with different values of  $k$ , which is the integrand of the Casimir formula (7). However, by plotting the value of this integrand with respect to different values of  $ik$ , we found that this function is exponentially decays with increasing the imaginary wavenumber  $ik$  (see Figure 1) and with this property, we suggest using the normal trapezoidal rule to calculate the integral  $\int_0^\infty \Xi(ik) dk = \int_0^\infty \log \frac{\det V_{ik}}{\det \tilde{V}_{ik}} dk$ . The steps are sketched as follows.

- Set  $f(k) = \log \frac{\det V_{ik}}{\det \tilde{V}_{ik}}$  and the range of  $k$  is from 0 to  $\infty$ .
- Let  $k = -\log(y)$ , then the integral  $\int_0^\infty \log \frac{\det V_{ik}}{\det \tilde{V}_{ik}} dk$  becomes  $\int_0^\infty f(k) dk = \int_0^1 \frac{f(-\log(y))}{y} dy$ .
- Set the range of  $k$  as  $(lb, ub)^2$  and the corresponding range for  $y$  is  $(e^{-ub}, e^{-lb}) \subset [0, 1]$ .
- Choose  $m$  quadrature points from the interval  $(e^{-ub}, e^{-lb})$  and use the trapezoidal rule to evaluate the integral  $\int_{e^{-ub}}^{e^{-lb}} \frac{f(-\log(y))}{y} dy$ . Figure 2 plots the integrand with regard to new variable  $y (= e^{-k})$ .

---

<sup>2</sup>“ub” is short for upperbound and “lb” is short for lowerbound.

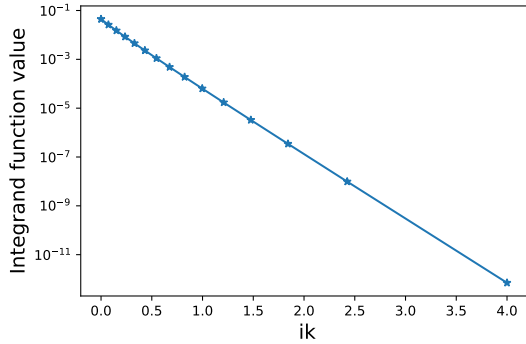


Figure 1: The integrand of the Casimir energy whose value exponentially decays with increasing imaginary wavenumber.

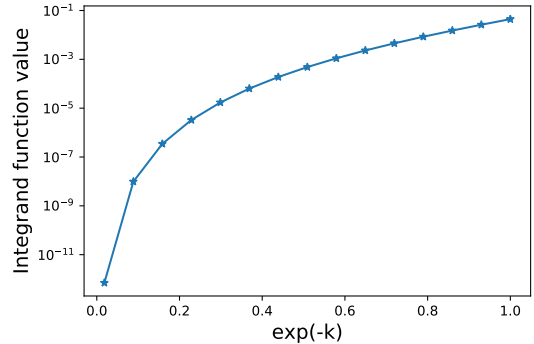


Figure 2: The integrand of the Casimir energy after changing the variable for applying the trapezoid quadrature rule.

### 3. Spectral property of the integral operators

The matrix  $M_\infty$  is a compact perturbation of matrix  $M$ , which makes the eigenvalues of them close to each other. Therefore, if we plot the eigenvalues of the matrix  $MM_\infty^{-1}$ , we can notice that there are many eigenvalues closed to 1 and nearly contributes nothing to the log determinant. This spectral property inspires us to use some iteration method to approximate the extreme eigenvalues of  $MM_\infty^{-1}$ . In order to make the computation process more efficiently, we will introduce an inverse-free method to speed up this process which makes us deal with the large-scale problem in the future.

### 4. Inverse-free methods for computing $\log \det(\mathbf{V}_{ik} \tilde{\mathbf{V}}_{ik}^{-1})$

By Section 2, to compute the Casimir energy, we need to evaluate  $\log \frac{\det \mathbf{V}_{ik}}{\det \tilde{\mathbf{V}}_{ik}} = \log \det(\mathbf{V}_{ik} \tilde{\mathbf{V}}_{ik}^{-1})$  with different values of  $k$ . In this section, an efficient inverse-free and a LU decomposition based method will be introduced to compute this log determinant.

The log determinant of the matrix  $\mathbf{V}_{ik} \tilde{\mathbf{V}}_{ik}^{-1}$  is equal to the sum of the logarithm of each eigenvalue of  $\mathbf{V}_{ik} \tilde{\mathbf{V}}_{ik}^{-1}$ . Since  $\tilde{\mathbf{V}}_{ik}$  is a compact perturbation of  $\mathbf{V}_{ik}$ , most of the eigenvalues are close enough to 1, which contributes nothing on the value of Casimir energy and this fact is shown in the Figure 3. Therefore, the computation process for the large-scale problem can become efficient if we only approximate the extreme eigenvalues which mainly contribute to the log determinant. In addition, we should also avoid directly computing the inverse of the matrix  $\tilde{\mathbf{V}}_{ik}$  since the computational complexity is cubic with respect to the matrix dimension.

In what follows, an inverse-free Krylov subspace method will be introduced to computed multiple smallest (or largest) eigenvalues of the generalized eigenvalue problems simultaneously. Afterwards, we will discuss another efficient method based on LU decomposition of the diagonal block matrix of  $\tilde{\mathbf{V}}_{ik}$ . Finally, the comparison of these two methods will be shown.

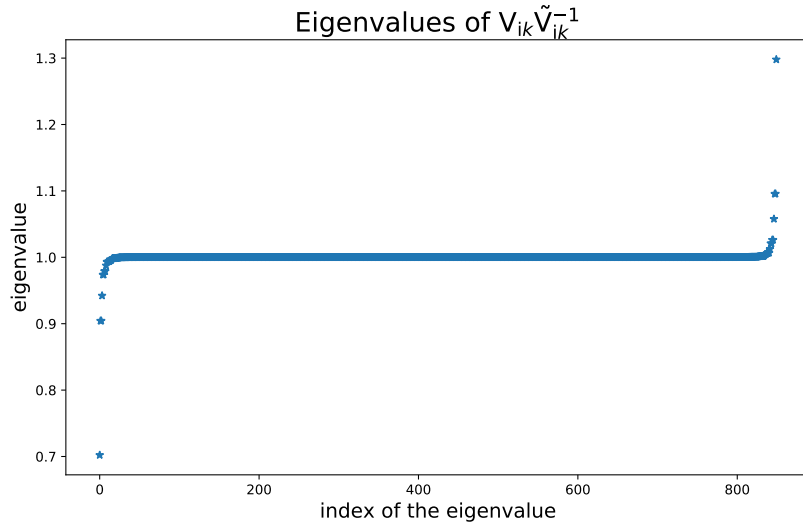


Figure 3: The eigenvalues of the matrix  $V_{ik}\tilde{V}_{ik}^{-1}$  when  $ik = 0.8i$ .

#### 4.1. Method I: Krylov subspace for generalized eigenvalue problem

Consider the eigenvalue problem:

$$V_{ik}\tilde{V}_{ik}^{-1}\mathbf{x} = \lambda\mathbf{x}, \quad (9)$$

where  $\lambda$  is the eigenvalue and  $\mathbf{x}$  is the corresponding eigenvalue. This eigenvalue problem is equivalent to the following generalized eigenvalue problem:

$$V_{ik}\tilde{\mathbf{x}} = \lambda\tilde{V}_{ik}\tilde{\mathbf{x}}. \quad (10)$$

Thus, we can focus on solving the problem (10) instead of (9) to avoid computing the matrix inversion. By [15], the authors proposed an inverse-free Krylov subspace method for computing multiple eigenvalues of the symmetric definite generalized eigenvalue problem simultaneously and the following algorithm summarizes this method.

---

**Algorithm 1:** Inverse-free Krylov subspace method for computing  $p$  smallest eigenvalues of the generalized eigenvalue problem  $A\mathbf{x} = \lambda B\mathbf{x}$

---

Input: Symmetric matrix  $A \in \mathbb{R}^{n \times n}$ , s.p.d matrix  $B \in \mathbb{R}^{n \times n}$  and a  $B$ -orthonormal matrix  $X^{(1)} \in \mathbb{R}^{n \times p}$  with  $X^{(1)*}BX = I_p$  and  $m \geq 1$

Output: The approximated  $p$  smallest eigenvalues of  $A\mathbf{x} = \lambda B\mathbf{x}$

- 1: Set  $\Theta^{(1)} = \text{diag}(X^{(1)*}AX^{(1)})$
  - 2: **for**  $k = 1, 2, \dots$  **do**
  - 3:   **for**  $i = 1, 2, \dots, p$  **do**
  - 4:     Construct a basis  $\hat{Z}_i$  of the  $i$ th Krylov subspace  $K_m(A - \theta_i^{(k)}B, x_i^{(k)})$  with dimension  $m$
  - 5:     Orthonormalize  $[\hat{Z}_1 \cdots \hat{Z}_p]$  to obtain  $Z$
  - 6:     Project  $A$  and  $B$  on  $Z$ :  $A_m = Z^*AZ$ ,  $B_m = Z^*BZ$
  - 7:     Compute  $p$  smallest eigenpairs  $(\theta_i, u_i)$ ,  $1 \leq i \leq p$  of the matrix pencil  $(A_m, B_m)$
  - 8:      $\Theta^{(k+1)} = \text{diag}(\theta_1, \dots, \theta_p)$ ;  $X^{(k+1)} = ZU$ ,  $U = (u_1 \cdots u_p)$
  - 9:   **end for**
  - 10: **end for**
- 

Algorithm 1 can make us approximate  $p$  smallest eigenvalues of the matrix pencil  $(A, B)$  and the most trivial way to compute the  $p$  largest eigenvalues is to use the same algorithm as above but only change the matrix  $M$  to  $-M$ . Then we can find the  $p$  smallest eigenvalues of  $(-A, B)$  and by adding the negative sign in front of these eigenvalues, we can obtain  $p$  largest eigenvalues of  $(A, B)$ .

We denote the  $p$  smallest (or largest) eigenvalues obtained from this method as

$$\Lambda_{\text{inv\_free}}^{\text{smallest}} = \left\{ \lambda_0^{(s)}, \lambda_1^{(s)}, \dots, \lambda_{p-1}^{(s)} \right\}, \quad (11)$$

$$\Lambda_{\text{inv\_free}}^{\text{largest}} = \left\{ \lambda_0^{(l)}, \lambda_1^{(l)}, \dots, \lambda_{p-1}^{(l)} \right\}. \quad (12)$$

Then, the value of  $\log \det(\mathbf{V}_{ik} \tilde{\mathbf{V}}_{ik}^{-1})$  can be approximated by

$$\log \det(\mathbf{V}_{ik} \tilde{\mathbf{V}}_{ik}^{-1}) \approx \sum_{i=0}^p \log \left( \lambda_i^{(s)} \right) + \sum_{i=0}^p \log \left( \lambda_i^{(l)} \right)$$

#### 4.2. Method II: LU decomposition for inverting the matrix

Another inverse-free way to compute  $\log \det(\mathbf{V}_{ik} \tilde{\mathbf{V}}_{ik}^{-1})$  is to find the  $LU$  decomposition for each diagonal block matrix and solve the linear system on each subdomain. To be specific, the inverse of the matrix  $\tilde{\mathbf{V}}_{ik}$  is

$$\tilde{\mathbf{V}}_{ik}^{-1} = \tilde{\mathbf{V}}(\mathbf{i}k)^{-1} = \begin{bmatrix} \mathbf{V}_{11}(\mathbf{i}k) & 0 & \cdots & 0 \\ 0 & \mathbf{V}_{22}(\mathbf{i}k) & \cdots & 0 \\ \vdots & \vdots & \ddots & \vdots \\ 0 & 0 & \cdots & \mathbf{V}_{NN}(\mathbf{i}k) \end{bmatrix}^{-1} = \begin{bmatrix} \mathbf{V}_{11}^{-1}(\mathbf{i}k) & 0 & \cdots & 0 \\ 0 & \mathbf{V}_{22}^{-1}(\mathbf{i}k) & \cdots & 0 \\ \vdots & \vdots & \ddots & \vdots \\ 0 & 0 & \cdots & \mathbf{V}_{NN}^{-1}(\mathbf{i}k) \end{bmatrix}$$

We can compute  $LU$  decomposition of each diagonal block matrix  $\mathbf{V}_{ii} = \mathbf{V}_{ii}(\mathbf{i}k)$  for  $i = 1, 2, \dots, N$  and the decomposition is written as  $\mathbf{V}_{ii} = \mathbf{L}_{ii} \mathbf{U}_{ii}$ , where  $\mathbf{L}_{ii}$  is a lower triangular matrix and  $\mathbf{U}_{ii}$  is upper triangular. Afterwards, we solve the linear system  $\mathbf{L}_{ii} \mathbf{U}_{ii} \mathbf{x}_j = \mathbf{e}_j$ , for  $j = 1, 2, \dots, N_{\mathbf{V}_{ii}}$ , where  $\mathbf{e}_j$  denotes the vector with a 1 in the  $j$ th coordinate and 0's elsewhere and  $N_{\mathbf{V}_{ii}}$  is the dimension of the block  $\mathbf{V}_{ii}$ . Finally, the inverse of  $\mathbf{V}_{ii}$  is  $\mathbf{V}_{ii}^{-1} = [\mathbf{x}_1 \ \cdots \ \mathbf{x}_{N_{\mathbf{V}_{ii}}}]$  and we can notice that this whole process contains no step that needs us to compute the inverse of any matrix.

We denote the inverse of the matrix  $\tilde{\mathbf{V}}_{ik}$  computed by the above inverse-free  $LU$  decomposition method as  $\tilde{\mathbf{V}}_{ik}^{-1,\text{LU}}$  and to approximate multiple extreme eigenvalues of  $\mathbf{V}_{ik} \tilde{\mathbf{V}}_{ik}^{-1,\text{LU}}$ , we would like to firstly construct the Krylov subspace  $K_m(\mathbf{V}_{ik} \tilde{\mathbf{V}}_{ik}^{-1,\text{LU}}, \mathbf{b})$ , where  $\mathbf{b}$  is some initial vector and  $m$  is the dimension of this subspace. Afterwards, we implement the Arnoldi iteration to obtain the orthogonal basis of this  $m$ th Krylov subspace and project the matrix  $\mathbf{V}_{ik} \tilde{\mathbf{V}}_{ik}^{-1,\text{LU}}$  onto this basis. This projection matrix is called the Hessenberg matrix and we denote it as  $H_m$ . By [16], the eigenvalues of  $H_m$  (which are also called Ritz eigenvalues) can give good approximations to some eigenvalues of  $\mathbf{V}_{ik} \tilde{\mathbf{V}}_{ik}^{-1,\text{LU}}$ . Therefore, we denote the eigenvalues of  $H_m$  as

$$\Lambda_{\text{Arno}} = \left\{ \lambda_0^{(\text{Arno})}, \lambda_1^{(\text{Arno})}, \dots, \lambda_{m-1}^{(\text{Arno})} \right\} \quad (13)$$

and the value of  $\log \det(\mathbf{V}_{ik} \tilde{\mathbf{V}}_{ik}^{-1})$  can be approximated by

$$\log \det(\mathbf{V}_{ik} \tilde{\mathbf{V}}_{ik}^{-1}) \approx \sum_{i=0}^{m-1} \log \left( \lambda_i^{(\text{Arno})} \right).$$

#### 4.3. Comparison of two inverse-free methods

Figure 4 plots multiple smallest and largest approximated eigenvalues of the matrix  $\mathbf{V}_{ik} \tilde{\mathbf{V}}_{ik}^{-1}$  when  $p = 25$  (for  $p$  in Method I) and the dimension of the Krylov subspace in both line four of Algorithm 1 and Method II is  $m = 50$ .

### Compare the exact eigenvalues of $V_{ik}\tilde{V}_{ik}^{-1}$ with approximated ones ( $m = 50$ )

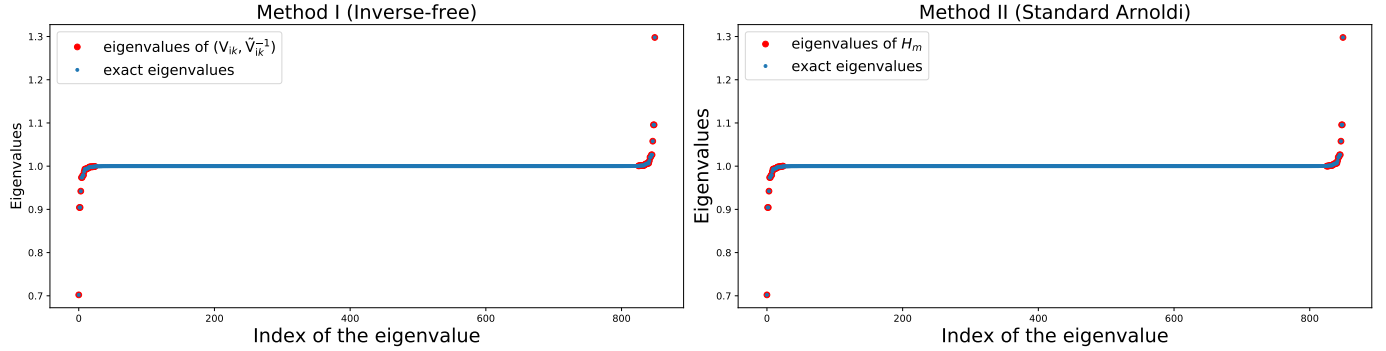


Figure 4: Comparison between  $p$  approximated smallest eigenvalues and  $p$  largest ones with the exact eigenvalues when  $p = 25$  and the dimension of the Krylov subspace in both line four of Algorithm 1 and Method II is set as  $m = 50$ .

By Figure 4, the approximated extreme eigenvalues are quite close to the exact ones and in order to see how close they are, we plot the relative error between them in Figure 5.

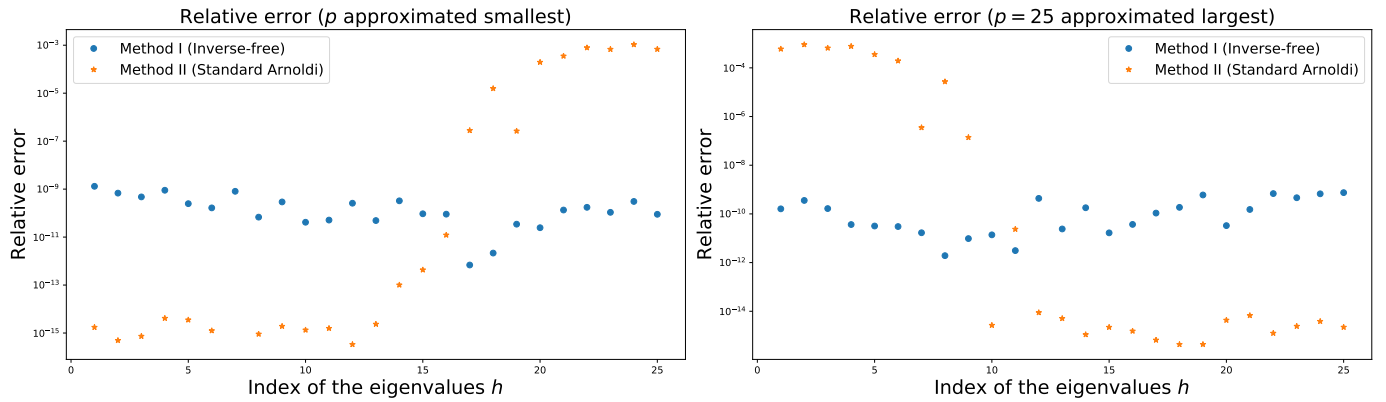


Figure 5: (Left) The relative error of the  $p$  ( $p = 25$ ) smallest eigenvalues between the exact and approximated ones. (Right) The relative error of the  $p$  ( $p = 25$ ) largest eigenvalues between the exact and approximated ones.

To more intuitively see which inverse-free method is better, we would like to fix the dimension of the Krylov subspace as  $m = 50$  and increase the number of the approximated eigenvalues from 2 to 50 and then plot the relative error in each case. The procedure is as follows.

For example, when the number of the approximated eigenvalue is 2, the relative error for the Method I (inverse-free) is computed by:

$$\text{Err}_{\text{inv\_free}}^{(2)} = \frac{\left(\log(\lambda_0^{(s)}) + \log(\lambda_{p-1}^{(l)})\right) - \text{exact\_logdet}}{\text{exact\_logdet}},$$

where `exact_logdet` is the exact value of the log determinant of  $V_{ik}\tilde{V}_{ik}^{-1}$  and  $\lambda_0^{(s)}, \lambda_{p-1}^{(l)}$  are from the sorted sets  $\Lambda_{\text{inv\_free}}^{\text{smallest}}$  in (11) and  $\Lambda_{\text{inv\_free}}^{\text{largest}}$  in (12), respectively; and the relative error for the Method II (standard Arnoldi) is computed by

$$\text{Err}_{\text{Arno}}^{(2)} = \frac{\left(\log(\lambda_0^{\text{Arno}}) + \log(\lambda_{m-1}^{\text{Arno}})\right) - \text{exact\_logdet}}{\text{exact\_logdet}},$$

where  $\lambda_0^{\text{Arno}}$  and  $\lambda_{m-1}^{\text{Hess}}$  are both from the sorted set  $\Lambda_{\text{Arno}}$  in (13).

The following graph plots the relative error computed in both cases and we can see that their relative errors shares the same trend at the beginning and the Method II (Hessenberg) becomes worse when the number of the approximated eigenvalues becomes close to the dimension of the Krylov subspace.

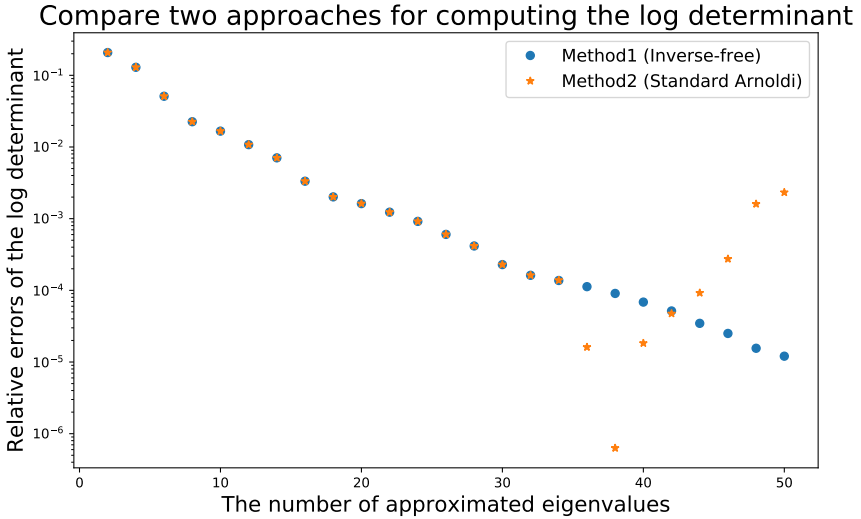


Figure 6: The comparison between two inverse-free methods by fixing the dimension of the Krylov subspace as  $m = 50$  and increasing the number of the approximated eigenvalues from 2 to 50.

## 5. Numerical experiments

In this section, we are going to show the numerical results for computing the Casimir energy between two perfectly conducting objects, which are spheres, menger sponges, ice crystals and ellipsoids. The reference value of the Casimir energy is computed by the Richardson extrapolation method which is often used for obtaining the higher-order estimate at zero grid spacing. Denote  $\mathcal{E}_{\text{fine}}$  and  $\mathcal{E}_{\text{coarse}}$  as the Casimir energy numerically computed from the formula (7) by setting the grid size  $h$  as  $h_{\text{fine}}$  and  $h_{\text{coarse}}$  ( $h_{\text{fine}} < h_{\text{coarse}}$ ), separately. Then, the high-accuracy result  $\mathcal{E}_{\text{exact}}$  can be generated from the following formula:

$$\mathcal{E}_{\text{exact}} \approx \mathcal{E}_{\text{fine}} + \frac{h_{\text{coarse}}^2 \mathcal{E}_{\text{fine}} - h_{\text{fine}}^2 \mathcal{E}_{\text{coarse}}}{h_{\text{coarse}}^2 - h_{\text{fine}}^2}. \quad (14)$$

In addition, the asymptotic series of the Casimir energy are also available in two spheres' case and the series can be found in [8] for both equal and unequal radii's cases.

### 5.1. Two spheres case

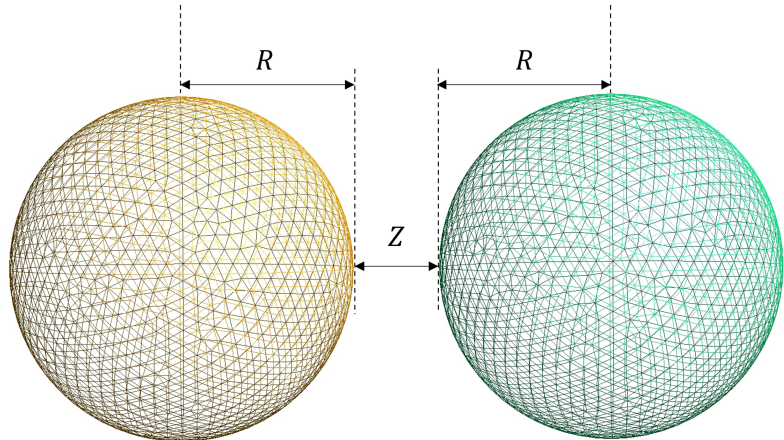


Figure 7: Two spheres with equal radii:  $R$  represents the radius of the spheres and  $Z$  is the distance between them.

Consider two perfectly conducting spheres with equal radii, which are shown in the Figure 7. Inside the figure,  $R$  is the radius of the spheres and the distance between them is denoted as  $Z$ . We begin with estimating the Casimir energy between two spheres with radius  $R = 1$  at the distance of  $Z$  via the formula (7) in two different refinement levels:  $h_{\text{fine}} = 0.05$  and  $h_{\text{coarse}} = 0.1$  and the distance  $Z$  between them is ranging from 0.5 to 3.0. Afterwards, the extrapolation result can be obtained by substituting these Casimir energy estimates into the formula (14). This result would be regarded as the exact value of the Casimir energy and can be used to compare with the estimates derived from the asymptotic series introduced below.

According to [8], the Casimir energy between two spheres (with equal radii  $R$ ) at asymptotically large separations can be obtained as a series in terms of the ratio of centre distance  $L$  ( $L = 2R + Z$ ) to sphere radius  $R$ :

$$\mathcal{E} = -\frac{\hbar c}{\pi} \frac{1}{L} \sum_{n=0}^{\infty} b_n \left( \frac{R}{L} \right)^{n+2}, \quad (15)$$

where the first six coefficients are  $b_0 = -1/4$ ,  $b_1 = -1/4$ ,  $b_2 = -77/48$ ,  $b_3 = -25/16$ ,  $b_4 = -29837/2880$ ,  $b_5 = -6491/1152$ . Figure 8 shows the comparison between the Casimir energy computed from asymptotic series (15) and the exact value evaluated through Richardson extrapolation. Here, we observe that the asymptotic value gradually approaches to the exact value as the distance  $Z$  increases since the asymptotic expansion (15) only works when the distance between two spheres is asymptotically large.

## Two spheres with equal radii

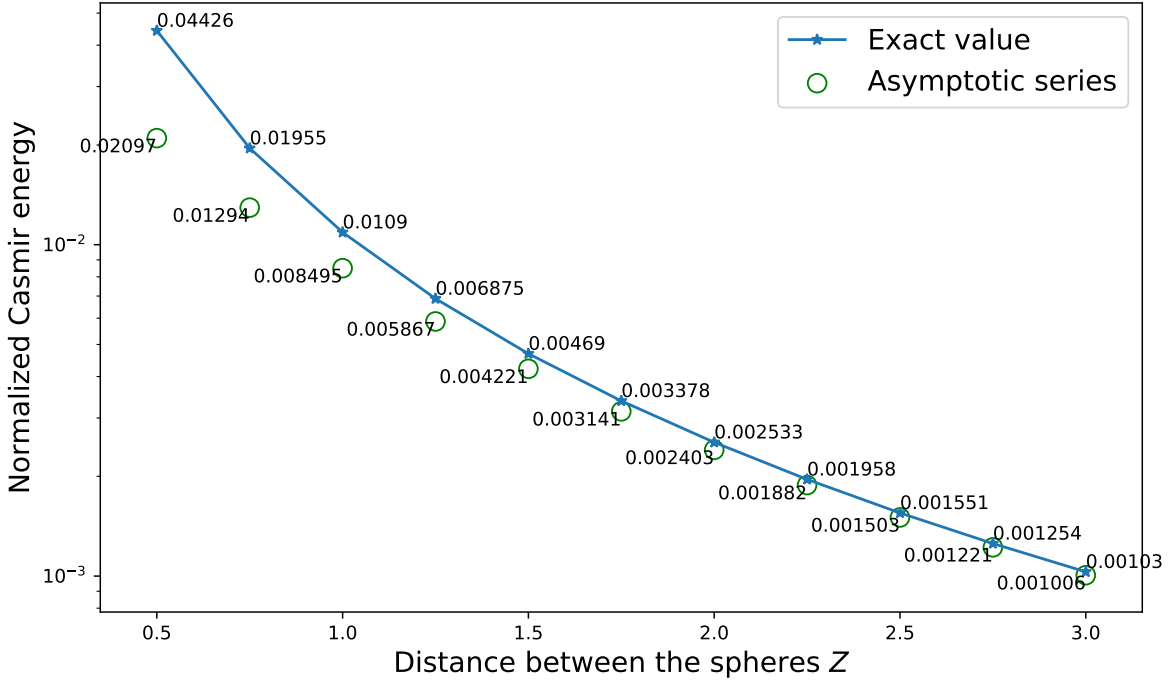


Figure 8: Normalized Casimir energy<sup>3</sup> in two spheres with equal radii's case. The radius is  $R = 1$  and the distance  $Z$  ranges from 0.5 to 3.0. The exact value of the (normalized) Casimir energy has been written beside the data point, which is round up to 4 significant digits.

Afterwards, in order to test the performance of the two efficient methods introduced in Section 4, we would use them to evaluate the Casimir energy between two spheres described above. For the inverse-free Krylov subspace method, the dimension of the Krylov subspace is set as  $m = 20$  and 50 and the number of

<sup>3</sup>The normalized Casimir energy is  $\mathcal{E}/\hbar c$ , for  $\mathcal{E}$  defined in (7).

approximated smallest (or largest) eigenvalues is  $p = 10$  and  $25$ , respectively. For the standard Arnoldi method, the dimension of the Krylov subspace is also set as  $m = 20$  and  $50$ .

Figure 9 shows the relative distance between the estimates computed through inverse-free Krylov subspace method (dashed/solid green triangles), standard Arnoldi method (dashed/solid blue circles), asymptotic series (solid black square) and the exact values. Here, we can easily see that the inverse-free Krylov subspace method behaves better than the standard Arnoldi method no matter when the dimension  $m$  is  $20$  or  $50$  and as we increase the Krylov subspace dimension, the relative error decreases.

In addition, it can be noticed that when the distance  $Z$  between the spheres increases, the relative error for both methods goes down. The reason appears to be that the cross interaction between them becomes weaker as the spheres are getting away from each other. This leads the compact perturbation  $\tilde{V}_k$  to become close to  $V_k$ , which reduces the number of the eigenvalues that mainly contribute on the log determinant of  $V_k \tilde{V}_k^{-1}$ . Therefore, if we keep setting the same dimension of Krylov subspace for the spheres are at a large distance, we would have a better approximation on the Casimir energy.

## Two spheres with equal radii

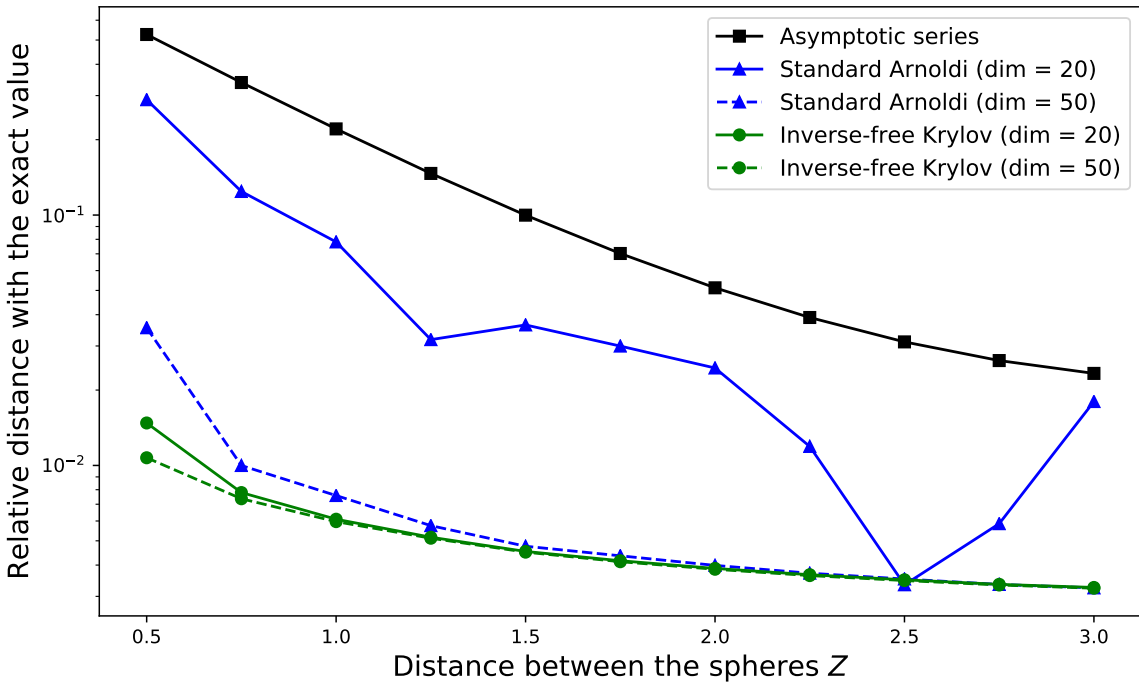


Figure 9: Relative distance between the reference value (computed by Richardson extrapolation) with the asymptotic series (solid black square) and the estimates evaluated from the standard Arnoldi method (dashed/solid blue circles) and inverse-free Krylov subspace method (dashed/solid green triangles) by setting the dimension of the Krylov subspace as  $m = 20$  and  $50$  and for the inverse-free Krylov subspace method, the number of the approximated smallest (or largest) eigenvalues is set as  $p = 10$  and  $25$ , respectively.

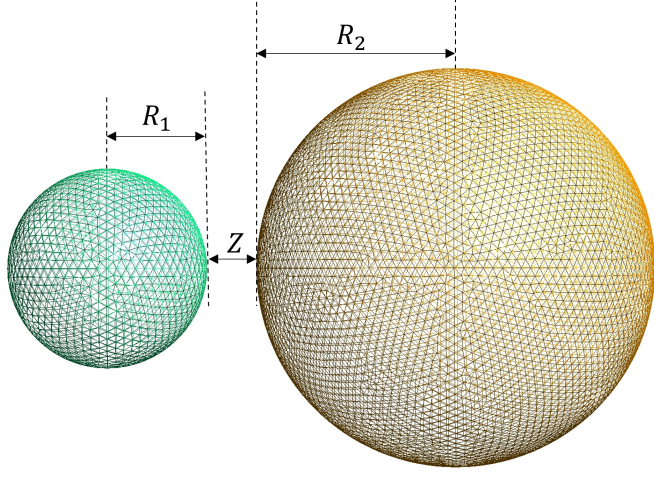


Figure 10: Two spheres with unequal radii:  $R_1$  and  $R_2$  represent the radius of the spheres and  $Z$  is the distance between them.

When the perfectly conducting spheres have different radii  $R_1, R_2$  (see Figure 10) and the centre distance is denoted as  $L = R_1 + R_2 + Z$ , the asymptotic expansion of the Casimir energy at asymptotically large distance can be written as:

$$\mathcal{E} = -\frac{\hbar c}{\pi} \frac{1}{L} \sum_{n=0}^{\infty} \tilde{b}_n(\eta) \left( \frac{R_1}{L} \right)^{n+2}, \quad (16)$$

where the coefficients  $\{\tilde{b}_n\}$  depend on the parameter  $\eta = R_2/R_1$  and the first six coefficients are

$$\begin{aligned} \tilde{b}_0 &= -\frac{\eta}{4}, & \tilde{b}_1 &= -\frac{\eta + \eta^2}{8}, & \tilde{b}_2 &= -\frac{34(\eta + \eta^3) + 9\eta^2}{48}, & \tilde{b}_3 &= -\frac{2(\eta + \eta^4) + 23(\eta^2 + \eta^3)}{32}, \\ \tilde{b}_4 &= -\frac{8352(\eta + \eta^5) + 1995(\eta^2 + \eta^4) + 38980\eta^3}{5760}, & \tilde{b}_5 &= -\frac{-1344(\eta + \eta^6) + 5478(\eta^2 + \eta^5) + 2357(\eta^3 + \eta^4)}{2304}. \end{aligned}$$

In the following experiment, the radii of the spheres shown in Figure 10 are set as  $R_1 = 0.5$  and  $R_2 = 1$ . As in the previous example, the exact value of the Casimir energy is computed through the Richardson extrapolation formula (14), where the coarse and fine grid size are  $h_{\text{coarse}} = 0.1$  and  $h_{\text{fine}} = 0.05$ , separately. In this case, the asymptotic value of the Casimir energy was estimated by the series (16) and the comparison between the exact value and asymptotic one is shown in Figure 11. Again we see that when the distance between two spheres decreases, the asymptotic value gets close to the exact one and the reason for this is clearly stated in the above equal radii's case.

## Two spheres with unequal radii

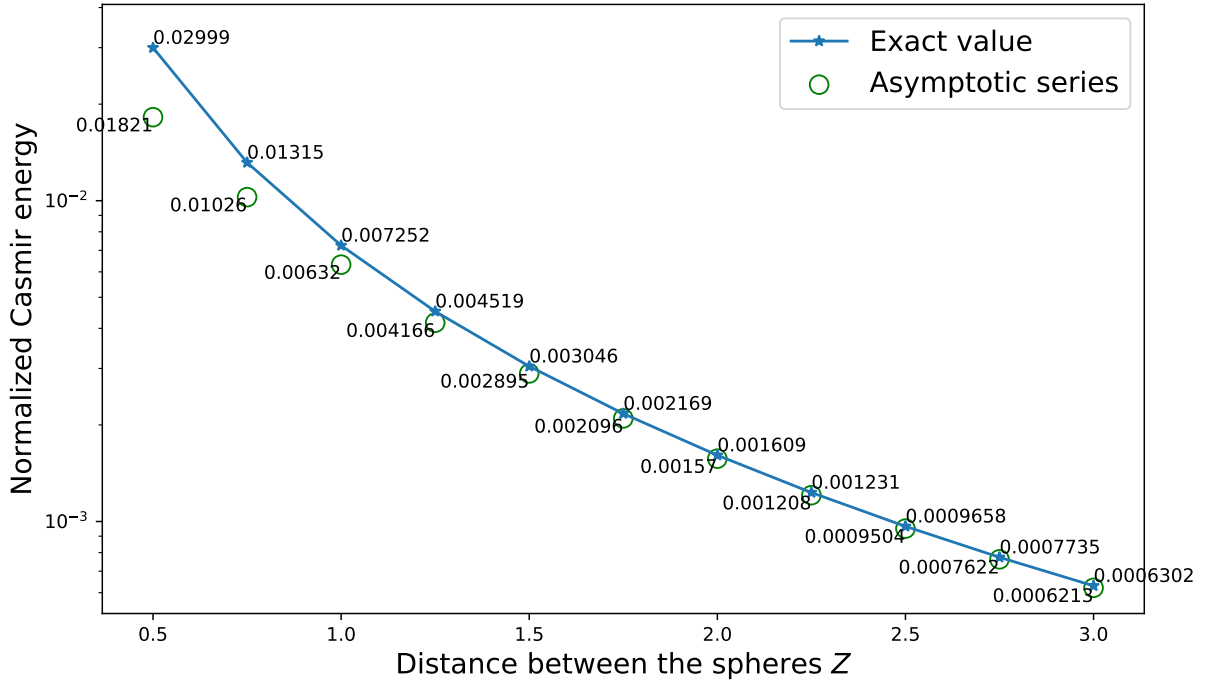


Figure 11: Normalized Casimir energy in two spheres with unequal radii's case. The radius is  $R = 1$  and the distance  $Z$  ranges from 0.5 to 3.0. The exact value of the (normalized) Casimir energy has been written beside the data point, which is round up to 4 significant digits.

By keeping all the experimental settings being the same with the equal radii's case, the numerical experiments on testing the performance of the inverse-free and standard Arnoldi methods have been done in the unequal radii's case and the results are shown in Figure 12, from which we observe that the results between these two efficient methods have no big difference except the standard Arnoldi case when the dimension  $m = 20$ . Compared with the previous case, it is supposed to be due to the smaller scatterer, leading to the smaller number of eigenvalues that makes significant influence on the log determinant.

## Two spheres with unequal radii

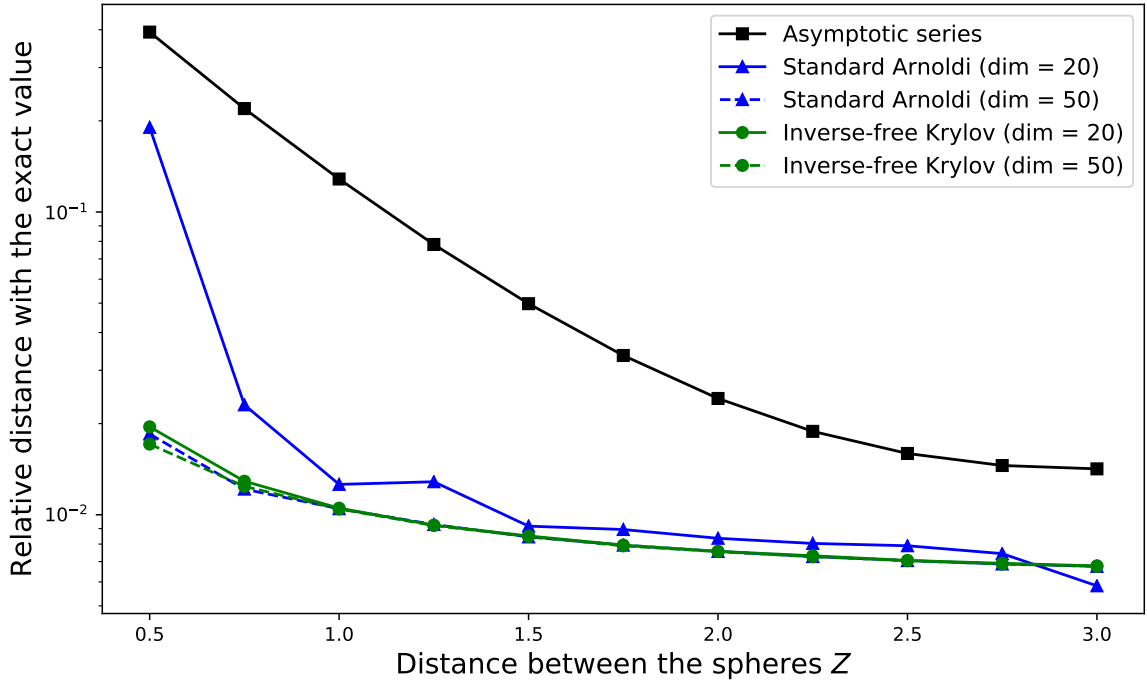


Figure 12: Relative distance between the reference value (computed by Richardson extrapolation) with the asymptotic series (solid black square) and the estimates evaluated from the standard Arnoldi method (dashed/solid blue circles) and inverse-free Krylov subspace method (dashed/solid green triangles) by setting the dimension of the Krylov subspace as  $m = 20$  and  $50$  and for the inverse-free Krylov subspace method, the number of the approximated smallest (or largest) eigenvalues is set as  $p = 10$  and  $25$ , respectively.

### 5.2. Realistic objects case

In this part, the Casimir energy between the objects with special shapes such as the menger sponges, ice crystals and ellipsoids will be computed and the values labelled in the following figures are always round up to 4 significant digits.

Figure 13 plots the menger sponges in different levels (0, 1 and 2) and the length of these sponges is always 1. Afterwards, the Casimir energy between two menger sponges in the same level are plotted in Figure 14. By comparing the data point in these subfigures, it is easy to find that the Casimir energy decreases as the number of the iteration increases since the cross-sectional area gets smaller.

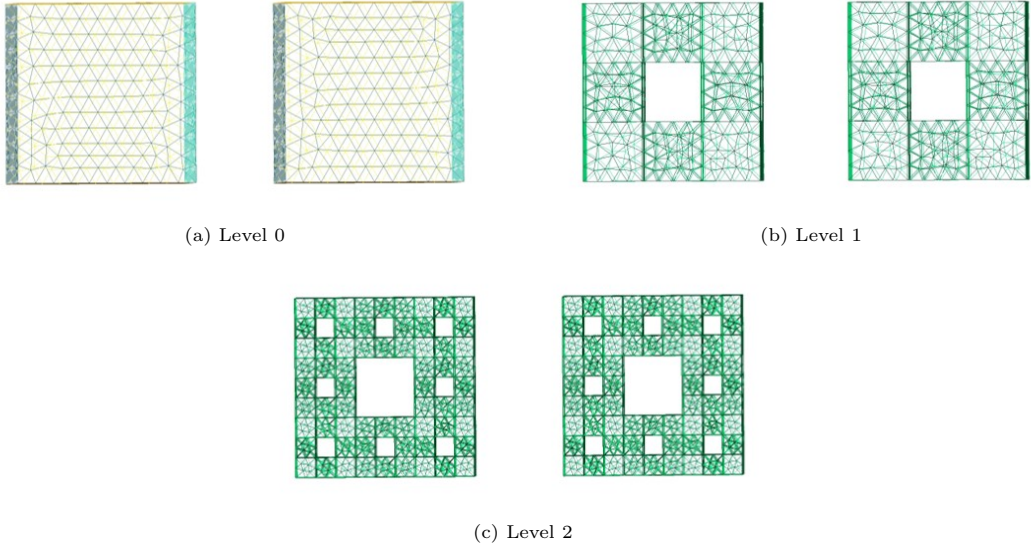


Figure 13: Menger sponges in different levels. The length of each sponge is 1.

Casimir energy between two menger sponges in different levels

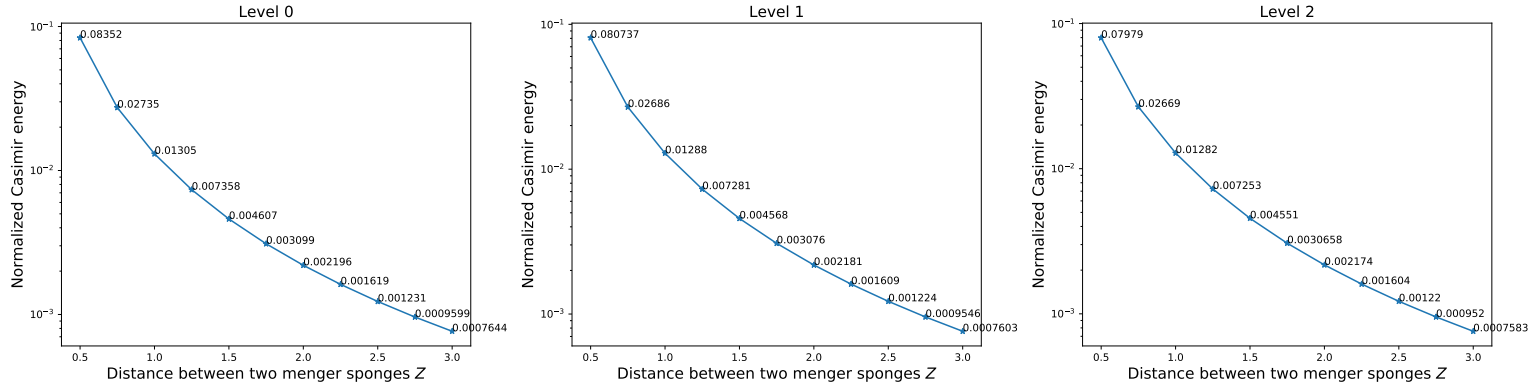


Figure 14: Normalized Casimir energy in two menger sponges' case. The length of each sponge is 1.

In the next example, the scatterers are ice crystals with different number of branches ranging from 2 to 6 (see Figure 15). By Figure 16, when the number of branches increases from 2 to 4, the Casimir energy increases as expected. But when the branches number added up to 5 and 6, the Casimir energy is much smaller since the main cross-sectional part cannot be as close as the 2, 3, 4-branches cases.

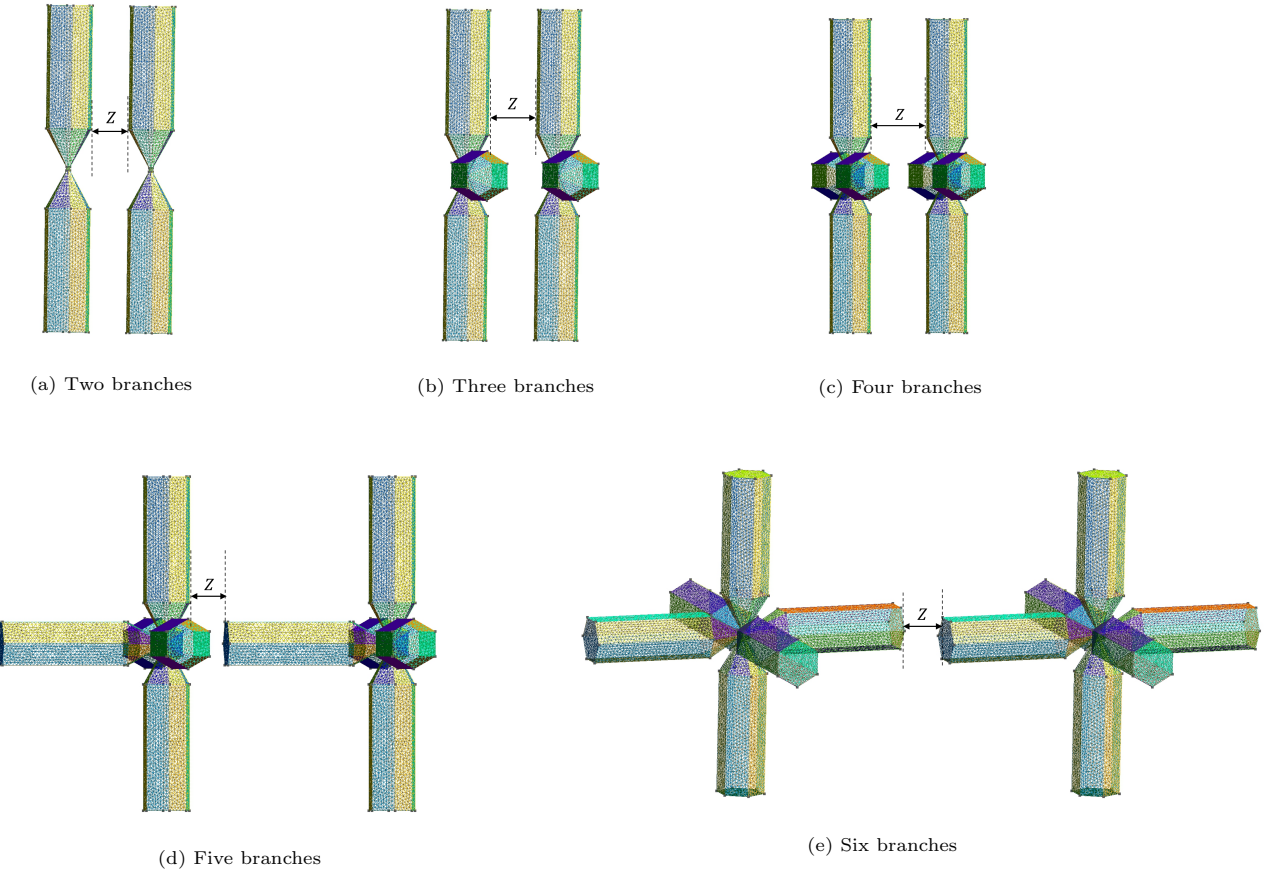


Figure 15: Ice crystals with different number of branches

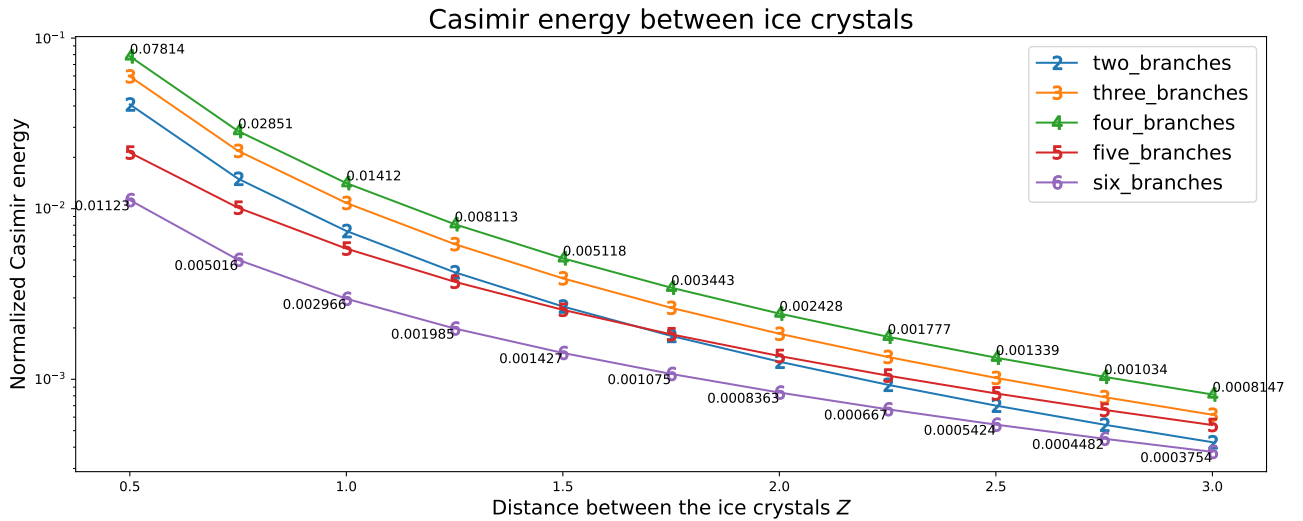


Figure 16: Normalized Casimir energy in ice crystals' case. To make the figure keep clear, only the 4-branches and 6-branches's case data points are labelled in the figure.

It is not hard to imagine that the Casimir energy would be different after the scatterers rotate while keeping the distance between them unchanged. Therefore, in the last example, we would see how the Casimir energy between two identical ellipsoids changes as one of the ellipsoids rotates.

In Figure 17a, the above ellipsoid is centering at  $(0, 0, 0)$  and the points  $(0.5, 0, 0)$ ,  $(0, 1, 0)$  and  $(0, 0, 0.5)$  are located on this surface and if the distance between these two ellipsoids is denoted as  $Z$ , then the below one is centering at  $(0, 0, -(0.5 + 0.5 + Z))$  and the points  $(0.5, 0, -(0.5 + 0.5 + Z))$ ,  $(0, 1, -(0.5 + 0.5 + Z))$  and

$(0, 0, 0.5 - (0.5 + 0.5 + Z))$  are on it. Without rotation, the Casimir energy between them with different distance  $Z$  is plotted in Figure 18a.

To explore how the rotation affects the change of the Casimir energy, one can always keep one ellipsoid fixed and rotate the other one. The Figure 17b and 17c describe the case when one of the ellipsoids rotates around  $z$ - and  $x$ -axis, respectively. From the Figure 18b, the Casimir energy changes periodically since we rotate one ellipsoid around  $z$ - or  $x$ - axis by 360 degrees.

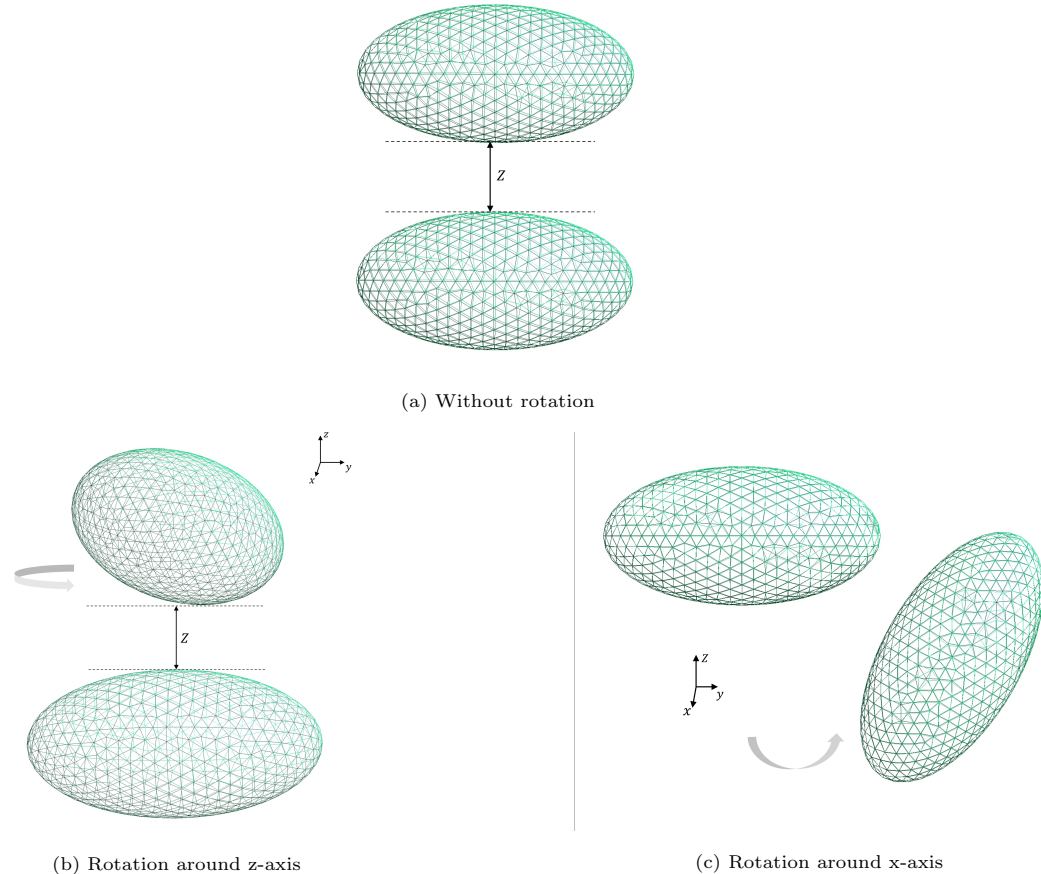
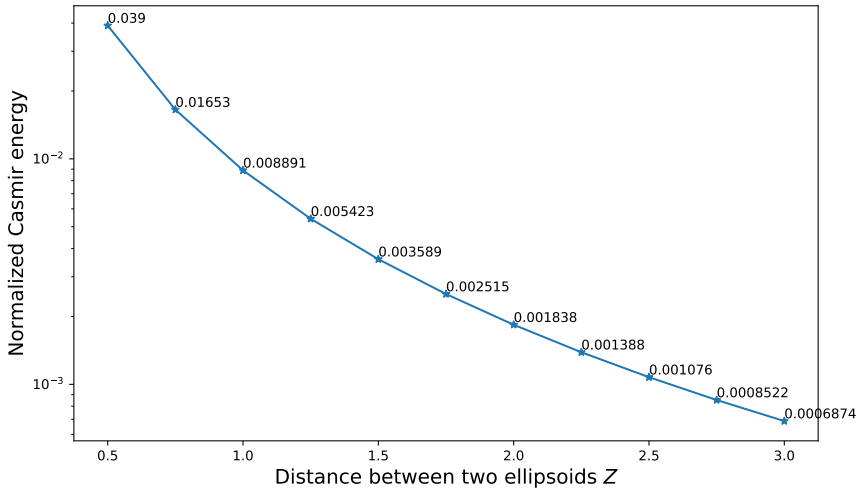


Figure 17: Two ellipsoids with or without rotation

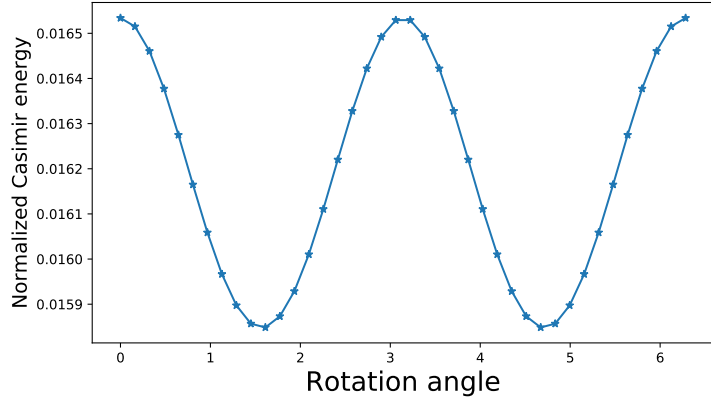
### Casimir energy between two ellipsoids



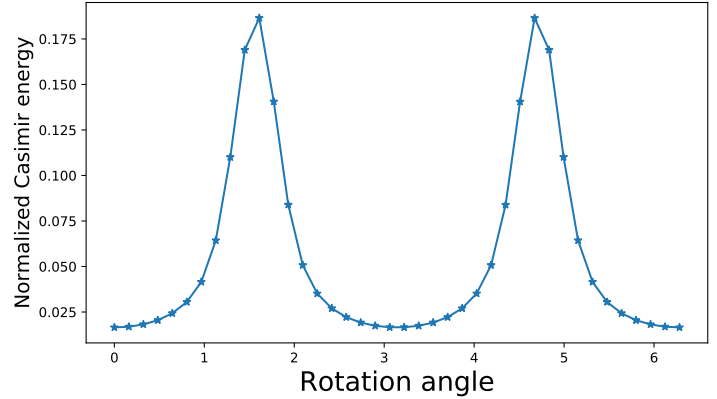
(a) Casimir energy between two ellipsoids with different distances

### Casimir energy between two ellipsoids with rotations

Rotate around z-axis



Rotate around x-axis



(b) Casimir energy when one of the ellipsoids rotates

Figure 18: The dependence of the Casimir energy and rotation angle of one of the ellipsoids.

## 6. Conclusion

## References

- [1] H. B. Casimir, On the attraction between two perfectly conducting plates, in: Proc. Kon. Ned. Akad. Wet., Vol. 51, 1948, p. 793.
- [2] I. E. Dzyaloshinskii, E. M. Lifshitz, L. P. Pitaevskii, The general theory of van der waals forces, Advances in Physics 10 (38) (1961) 165–209.
- [3] S. K. Lamoreaux, Demonstration of the casimir force in the 0.6 to 6  $\mu$  m range, Physical Review Letters 78 (1) (1997) 5.
- [4] T. Ederth, Template-stripped gold surfaces with 0.4-nm rms roughness suitable for force measurements: Application to the casimir force in the 20–100-nm range, Physical Review A 62 (6) (2000) 062104.

- [5] G. Bressi, G. Carugno, R. Onofrio, G. Ruoso, Measurement of the casimir force between parallel metallic surfaces, *Physical review letters* 88 (4) (2002) 041804.
- [6] D. Krause, R. Decca, D. López, E. Fischbach, Experimental investigation of the casimir force beyond the proximity-force approximation, *Physical review letters* 98 (5) (2007) 050403.
- [7] H. B. Chan, Y. Bao, J. Zou, R. Cirelli, F. Klemens, W. Mansfield, C. Pai, Measurement of the casimir force between a gold sphere and a silicon surface with nanoscale trench arrays, *Physical review letters* 101 (3) (2008) 030401.
- [8] T. Emig, N. Graham, R. Jaffe, M. Kardar, Casimir forces between compact objects: The scalar case, *Physical Review D* 77 (2) (2008) 025005.
- [9] T. Emig, N. Graham, R. Jaffe, M. Kardar, Casimir forces between arbitrary compact objects, *Physical review letters* 99 (17) (2007) 170403.
- [10] M. H. Reid, A. W. Rodriguez, J. White, S. G. Johnson, Efficient computation of casimir interactions between arbitrary 3d objects, *Physical review letters* 103 (4) (2009) 040401.
- [11] F. Hanisch, A. Strohmaier, A. Waters, A relative trace formula for obstacle scattering, arXiv preprint arXiv:2002.07291 (2020).
- [12] M. W. Scroggs, T. Betcke, E. Burman, W. Šmigaj, E. van't Wout, Software frameworks for integral equations in electromagnetic scattering based on calderón identities, *Computers & Mathematics with Applications* 74 (11) (2017) 2897–2914.
- [13] P. Waterman, New formulation of acoustic scattering, *The journal of the acoustical society of America* 45 (6) (1969) 1417–1429.
- [14] M. Ganesh, S. C. Hawkins, A far field based t-matrix method for three dimensional acoustic scattering, *ANZIAM Journal* 50 (2008) 121–136.
- [15] P. Quillen, Q. Ye, A block inverse-free preconditioned krylov subspace method for symmetric generalized eigenvalue problems, *Journal of computational and applied mathematics* 233 (5) (2010) 1298–1313.
- [16] Y. Saad, Numerical methods for large eigenvalue problems: revised edition, SIAM, 2011.